energies

MDPI

Article

Wind Characteristics in the Taiwan Strait: A Case Study of the First Offshore Wind Farm in Taiwan

Ke-Sheng Cheng [1,2,3], Cheng-Yu Ho [2,*] and Jen-Hsin Teng [4]

1 Department of Bioenvironmental Systems Engineering, National Taiwan University, Taipei 10617, Taiwan; rslab@ntu.edu.tw
2 Hydrotech Research Institute, National Taiwan University, Taipei 10617, Taiwan
3 Master Program in Statistics, National Taiwan University, Taipei 10617, Taiwan
4 Research and Development Center, Central Weather Bureau, Taipei 100006, Taiwan; tengjh@cwb.gov.tw
* Correspondence: cyho@ntu.edu.tw

Received: 4 November 2020; Accepted: 4 December 2020; Published: 9 December 2020

Abstract: This study analyzed the wind speed data of the met mast in the first commercial-scale offshore wind farm of Taiwan from May 2017 to April 2018. The mean wind speed and standard deviation, wind rose, histogram, wind speed profile, and diurnal variation of wind speed with associated changes in wind direction revealed some noteworthy findings. First, the standard deviation of the corresponding mean wind speed is somewhat high. Second, the Hellmann exponent is as low as 0.05. Third, afternoons in winter and nights and early mornings in summer have the highest and lowest wind speed in a year, respectively. Regarding the histogram, the distribution probability of wind is bimodal, which can be depicted as a mixture of two gamma distributions. In addition, the corresponding change between the hourly mean wind speed and wind direction revealed that the land–sea breeze plays a significant role in wind speed distribution, wind profile, and wind energy production. The low Hellmann exponent is discussed in detail. To further clarify the effect of the land–sea breeze for facilitating future wind energy development in Taiwan, we propose some recommendations.

Keywords: probability density function; bimodal; mixture distribution; monsoon; land–sea breeze; Hellmann exponent

1. Introduction

Wind energy is a sustainable renewable energy source with lower impact on the environment than fossil fuel burning. Nowadays, wind power is becoming increasingly ubiquitous in countries. In 2018, wind power accounted for 4.8% of global electricity. In 2019, the total installed capacity of wind turbines increased by 10% to 620 gigawatts (GW), of which the total installed capacity of offshore wind power was 27 GW, with a net increase of 5 GW (19%) [1,2]. The Taiwan Strait accounts for most of the top 20 offshore wind farm sites in the world, making it an excellent location for developing offshore wind power. The primary goal of Taiwan is to raise its offshore wind power capacity to 5.7 GW by 2025. Furthermore, for the next 10 years from 2026 to 2035, the goal is to install 1 GW per year [3,4].

Wind energy is an intermittent energy source. Although the annual power generated is roughly the same, it can vary greatly on shorter time scales, such as hourly, daily, or quarterly. The power supply system must always maintain a balance between instantaneous power generation and consumption to protect grid stability; hence, this variability introduces substantial challenges for integrating a large amount of wind energy into the grid system. Therefore, in addition to forecasting wind energy after operating wind farms, assessing wind energy potential before developing wind farms is essential.

To evaluate a potential wind farm site, wind characteristics of the site must be determined to correctly assess its wind energy potential and to subsequently improve the accuracy of wind energy prediction. Correspondingly, wind speed features vary based on location; probability distribution functions are usually well suited to represent observed wind speed data. The Weibull distribution represents the actual distribution of wind speed per hour or 10 min in many locations. However, many papers have proposed other more suitable probability distribution functions for certain areas [5–8]. Generally, Weibull distribution is unsuitable for wind fields with high calms and bimodal or even multimodal distribution caused by special climatic conditions.

The sea surface can provide more frequent and stronger winds than the land surface due to its lower friction and lower visual impact on the landscape. However, construction and maintenance costs are much higher for the sea surface than for the land surface. Therefore, the trend of modern utility-scale wind turbines is moving toward large designs because the foundation cost of offshore wind turbines and the transportation cost of large vessels required for construction and transportation are high. To reduce deployment costs, few but large offshore wind turbines have been installed [9]. Therefore, the blades of modern wind turbines are getting longer and larger, and hubs are getting higher and higher. For example, the blades of 6 megawatt (MW) wind turbines may increase to 154 m in diameter, hub height is approximately 105 m, the height range to which the blades sweep over is getting increasingly larger, and the wind speed gradient experienced by blades may become progressively complex. Hence, understanding the vertical profile of the horizontal wind is essential. The vertical gradient of wind speed depends on surface friction, mainly on the wave height of the sea surface. However, the wave height is also affected by wind speed. In addition, the vertical gradient is affected by atmospheric stability; thus, it is affected by the temperature difference between the sea surface and air over the sea surface.

Because the heat storage capacity of water is much larger than that of land, sea surface temperature presents seasonal variations rather than diurnal variations. In general, the thermal inertia of seawater results in the time shift of seawater temperature by more than 1 month relative to the annual change in atmospheric temperature.

Due to differences in thermal capacity between the sea and land surfaces and differences in the friction coefficient between the surfaces of the coastal area, diurnal variation occurs in the local wind. This is referred to as land–sea breeze. The angle of the land–sea breeze rotates. The rotation rate of the angle is related to (1) the Coriolis force, (2) thermally induced mesoscale pressure gradient force, and (3) synoptic-scale pressure gradient force [10].

The first commercial-scale offshore wind project of Taiwan is the Formosa 1 offshore wind farm installed 6 km offshore of Miaoli County in the Taiwan Strait over an area of 11 km^2. Because it is only approximately 6 km away from the coastline, land–sea breeze plays a significant role concerning the 128-MW offshore wind power station, comprising two 4-MW wind turbines and twenty 6-MW wind turbines in water depths between 15 and 30 m.

Taiwan's government has developed a three-phase development strategy to raise its offshore wind power capacity to 5.7 gigawatts (GW) by 2025. The strategies include phase 1: Subsidize demonstration wind farms, attract private investments; phase 2: Announce potential wind farms sites, accept applications from developers; and phase 3: Guide development of offshore zones and transform domestic supply chain into a full industry. All demonstration wind farms are scheduled to be completed by 2020. With the completion of the first demonstration wind farm, a detailed performance evaluation is imperative and can offer technical details and insightful experiences for the design and management in the subsequent phases.

Little research has been conducted on the first commercial-scale wind farm in the Taiwan Strait. Most research refers to the power system stability [11–15] and wind potential assessment over large areas [16,17]. Site-specific wind characteristics are crucial for choices of turbines and estimation of generated wind energy. The mean wind speed does not tell how often high winds occur, and thus, characterizing the probability distribution of the wind speed at the wind farm site is required for site

performance evaluation. This study aims to investigate the wind speed characteristics of the first offshore wind farm in Taiwan for further performance evaluation of the wind farm and providing insightful technical details for further wind energy development in Taiwan. Specific objectives of this study include: (1) characterizing and modeling the probability distribution of the at-site wind speed, (2) characterizing the seasonal variation of wind speed and wind direction, (3) investigating the major climatological factors that affect the at-site wind speed characteristics and the performance of the Taiwan Strait wind farms.

Our study analyzed the wind speed data of the mast of the Formosa 1 wind farm to first determine the wind characteristics of the wind farm to obtain the appropriate probability distribution function for preparing evaluation indexes of wind farms, such as annual energy production (AEP) and operating probability. The wind profile formed through the combination of wind speeds at different heights collected from field observation can then be used to calculate the blade stress and can serve as the basis for blade design and selection [18–20]. For evaluating the strength of land–sea breeze in the coastal area of Taiwan, indicators have been recommended, which can also be used as factors for site selection and wind energy forecast. Overall, the results may contribute some useful insights regarding offshore wind farm development in the Taiwan Strait in the future.

2. Data Source and Analysis Methods

Data used in this study were 10-min average wind speed measured from May 2017 to April 2018 by the met mast of the first commercial-scale offshore wind farm in Taiwan—Formosa I (operating from December 2019 to date). The met mast is located approximately 5 km away from Zhunan Township, Miaoli County (Figure 1). Anemometers and wind vanes are installed on the met mast at 10, 30, 50, and 90 m above the mean sea level.

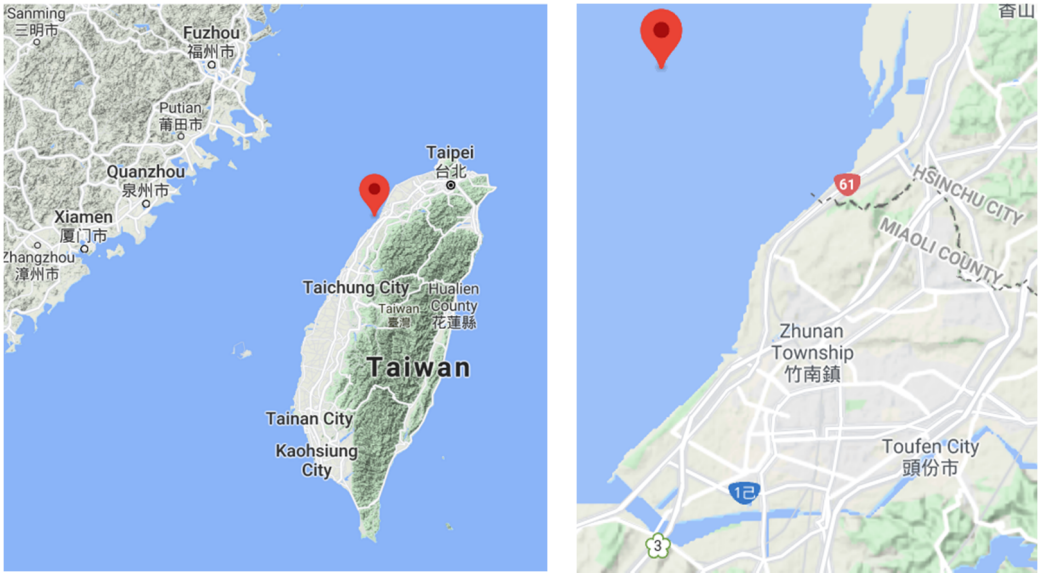

(**a**) (**b**)

Figure 1. (**a**) Location of the met mast (marked with a red pin); (**b**) the met mast and the coast area.

Winds highly vary spatially and temporally. Thus, understanding wind characteristics is essential for developing wind energy. Wind characteristics include the wind speed and direction. Furthermore, wind energy is related to the wind speed cube. Therefore, only through correctly estimating the wind speed can the wind energy potential be appropriately evaluated. Consequently, the probability density function is generally used to interpret the variation of wind speed with time and space. Regarding the wind direction, wind rose is often adopted to express its associated changes with the wind speed. Nevertheless, the most necessary and straightforward procedure is to evaluate the mean and standard

deviation. These statistical methods and preliminary analysis outcomes are briefly described in this section. In addition, the common land–sea breeze phenomenon in the coastal area is described.

2.1. Annual Mean and Standard Deviation of Wind Speed

The annual mean and standard deviation of 10-min mean wind speed are shown in Figure 2. The average wind speed at each height is almost the same (the annual average wind speed difference between the heights of 90 and 10 m is <1 m/s). Moreover, the Hellmann exponent (a) of the vertical profile of the horizontal wind described by power law is 0.05, which is less than that recommended by design codes or studies [21–26], and the spreading (standard deviation) of wind speed is quite large. Power law can be expressed as follows:

$$u(z) = u(z_r)\left(\frac{z}{z_r}\right)^a \tag{1}$$

where z_r is the reference height and a is the power law exponent.

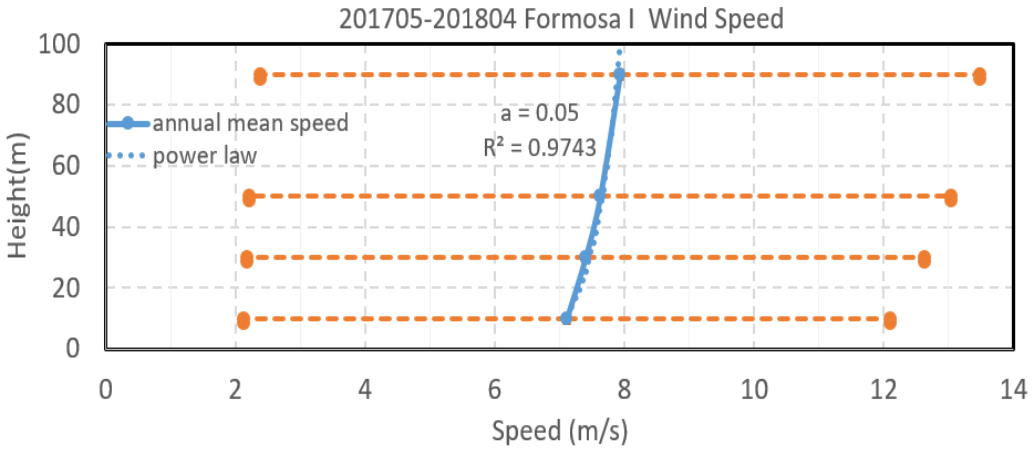

Figure 2. Annual mean speed (blue line) and standard deviation (orange dash line).

2.2. Probability Density Function of Wind Speed

Wind speed data have been modeled using different probability distribution functions including the Weibull, log-normal, gamma, Burr, Gumbel, and Rayleigh distributions [27–34]. Among these distributions, the Weibull distribution appears to be most widely used. In addition to the univariate modeling of wind speed data, various mixture distributions have also been used when the wind speed data exhibited a bimodal pattern [28,32,35]. Thus, in this study, the Weibull, mixture Weibull, and mixture gamma distributions were considered for probability density modeling of the wind speed data in Taiwan. The properties of the Weibull and gamma distributions and the maximum likelihood estimators of their parameters are briefly described in the following subsections.

2.2.1. Weibull Distribution

The probability density function and cumulative distribution function of a random variable X with the Weibull distribution are respectively given by

$$f_X(x) = \frac{\alpha}{\beta}\left(\frac{x}{\beta}\right)^{\alpha-1} exp\left[-\left(\frac{x}{\beta}\right)^{\alpha}\right] \tag{2}$$

$$F_X(x) = 1 - exp\left[-\left(\frac{x}{\beta}\right)^{\alpha}\right] \tag{3}$$

where α and β are the shape and scale parameters, respectively, and $x > 0,\ \alpha > 0$ and $\beta > 0$. The mean and variance of the Weibull distribution can also be expressed as the following functions of the scale and shape parameters,

$$E(X) = \mu = \beta\,\Gamma\left(1 + \frac{1}{\alpha}\right) \tag{4}$$

$$Var(X) = \sigma^2 = \beta^2\left[\Gamma\left(1 + \frac{2}{\alpha}\right) - \left(\Gamma\left(1 + \frac{1}{\alpha}\right)\right)^2\right] \tag{5}$$

where Γ represents the gamma function.

The scale and shape parameters can only be estimated using an observed sample. The method of moments (MOM) and the method of maximum likelihood (MML) are widely applied for parameters estimation. The former estimates the parameters of the underlying distribution by using the relationship between the population moments and the parameters and substituting the sample moments for the population moments. The latter maximizes the likelihood of observing the data, given the model. Generally speaking, the MOM estimators can be easily calculated, although they are often biased. By contrast, the maximum likelihood estimators (MLE) are more computationally intensive and often require numeric iterations. However, the maximum likelihood estimators are asymptotically normal and unbiased and have lower variance than other methods.

Given a random sample of size n, i.e., $x_1,\ x_2,\ \cdots,\ x_n$, the MLE of the shape and scale parameters of the Weibull distribution are as follows:

$$\hat{\beta} = \left(\frac{1}{n}\sum\nolimits_{i=1}^{n} x_i^{\hat{\alpha}}\right)^{1/\hat{\alpha}} \tag{6}$$

$$\frac{1}{\hat{\alpha}} = \frac{\sum_{i=1}^{n} x_i^{\hat{\alpha}} ln x_i}{\sum_{i=1}^{n} x_i^{\hat{\alpha}}} - \frac{1}{n}\sum_{i=1}^{n} ln x_i \tag{7}$$

The above MLE can only be estimated by numerical iteration.

2.2.2. Gamma Distribution

The probability density function and cumulative distribution function of the gamma distribution are respectively given by

$$f_X(x) = \frac{1}{\beta\Gamma(\alpha)}\left(\frac{x}{\beta}\right)^{\alpha-1} exp\left(-\frac{x}{\beta}\right),\ x > 0,\ \alpha > 0 \text{ and } \beta > 0 \tag{8}$$

$$F_X(x) = \frac{\gamma\left(\alpha, \frac{x}{\beta}\right)}{\Gamma(\alpha)} \tag{9}$$

where γ is the lower incomplete gamma function. The mean and variance of the gamma distribution can also be expressed as the following functions of the scale and shape parameters,

$$E(X) = \mu = \alpha\beta \tag{10}$$

$$Var(X) = \sigma^2 = \alpha\beta^2 \tag{11}$$

Given a random sample of size n, i.e., $x_1,\ x_2,\ \cdots,\ x_n$, the MLE of the shape and scale parameters of the gamma distribution are as follows [36,37]:

$$\hat{\alpha} = \begin{cases} \frac{1}{U}\left(0.500876 + 0.1648852U - 0.054427U^2\right) & 0 \le U \le 0.5772 \\ \frac{8.898919 + 9.05995U + 0.9775373U^2}{U(17.7928 + 11.968477U + U^2)} & 0.5772 \le U \le 17 \end{cases} \tag{12}$$

$$\hat{\beta} = \frac{\overline{x}_n}{\hat{\alpha}} \tag{13}$$

where $\overline{x}_n$ represents the sample mean and $U = ln\overline{x}_n - ln\left[(x_1 x_2 \cdots x_n)^{\frac{1}{n}}\right]$.

2.2.3. Mixture Distribution

The necessity of mixture distribution modeling arises from the situation when one samples from a population that consists of several homogeneous subpopulations, which are called the components of the population. For a k-component mixture distribution, let $f\left(x;\ \xi_j\right)$ represents the probability density function of the j-th subpopulation, with a parameter vector ξ_j, then the probability density function of the mixture population can be expressed by

$$g(x;\ \boldsymbol{\pi}, \boldsymbol{\phi}) = \sum_{j=1}^{k} \pi_j f\left(x;\ \xi_j\right) \tag{14}$$

where π_j is the proportion of the total population that is in the j-th component and is called the component weight. In the above equation, $\boldsymbol{\pi} = (\pi_1,\ \pi_2, \cdots, \pi_k)$ and $\boldsymbol{\phi} = (\xi_1,\ \xi_2, \cdots, \xi_k)$ together form the set of parameters of the mixture distribution. The weights satisfy the constraints that

$$\pi_j \geq 0 \text{ and } \sum_{j=1}^{k} \pi_j = 1 \tag{15}$$

Given a random sample of size n, i.e., $x_1,\ x_2,\ \cdots,\ x_n$, of a k-component mixture distribution, the maximum likelihood estimates, $\hat{\boldsymbol{\pi}}$ and $\hat{\boldsymbol{\phi}}$, are the parameter values that maximize the log-likelihood (ℓ) of the mixture distribution, i.e.,

$$\ell = \ln\left[\prod_{i=1}^{n}\left(\sum_{j=1}^{k} \hat{\pi}_j f\left(x_i; \hat{\xi}_j\right)\right)\right] = \sum_{i=1}^{n} \ln\left(\sum_{j=1}^{k} \hat{\pi}_j f\left(x_i; \hat{\xi}_j\right)\right) \tag{16}$$

The expectation-maximization (EM) algorithm has gained great popularity in calculating the maximum likelihood or maximum a posteriori (MAP) estimates of the mixture distribution parameters. The EM algorithm is an iterative numeric approach which involves two steps. The expectation (E) step assigns each observation to each subpopulation by using the current estimates of the parameters according to the relative density of the data points under each subpopulation. The maximization (M) step updates the estimates of the parameters by considering the expectation of a set of latent variables that represent the values of the parameter ξ corresponding to individually sampled components. Readers are referred to Lindsay [38] and Hastie et al. [39] for details of the EM algorithm.

2.3. Wind Rose

Figure 3 shows wind roses at 90-m height of a year, a summer month (June), a winter month (December), and a season transitional month (September).

Furthermore, Figure 3a shows that the prevailing wind is obvious, mainly in the direction of 30°, and the wind from the north-easterly direction (15–45°) accounts for most of the wind for approximately 40% of the year. The secondary direction is 215°, and the south-westerly wind (210–240°) accounts for most of the wind for approximately 20% of the year. The black portion in the figure represents the wind speed <4 m/s. Usually, wind turbines do not operate within this range. The blue portion shows the wind speed at 4–12 m/s; wind turbine blades begin to rotate but do not reach the full load. The yellow portion indicates that the wind speed is 12–25 m/s. As a rule, wind turbines adjust the pitch angle of their blades to maintain the rated load (full load). The red portion indicates that the wind speed has exceeded 25 m/s, and it is the point at which wind turbines normally shut down. According to the wind speed recorded at 90-m height, 147 times in a year, the 10-min mean wind speed exceeds 25 m/s, most of which occurs in October and November, when the north-east monsoon is rather strong, and in summer, only when typhoons strike.

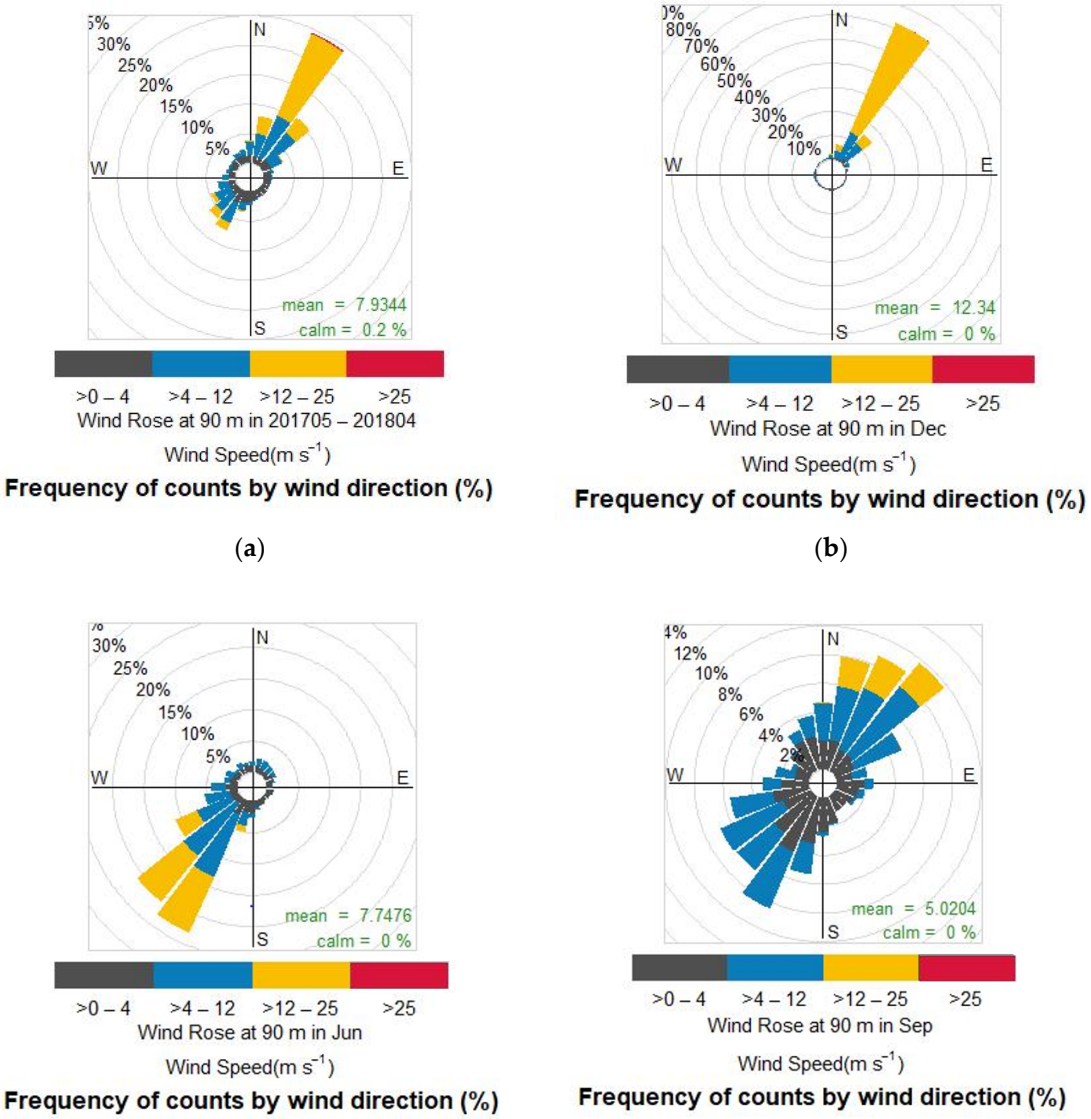

Figure 3. (**a**) Yearly wind rose; (**b**) wind rose of December 2017; (**c**) wind rose of June 2017; (**d**) wind rose of September 2017.

Figure 3b shows the wind rose of December. The wind direction is stable. In this month, 60% and 15% of 30° and 45° wind is present, respectively. In addition to the northeast wind direction, there is hardly any wind in other directions. Figure 3c shows the wind rose in June. Most of the wind comes from the southwest (210–240°). Figure 3d shows the wind rose in September. The northeast monsoon begins to prevail, but the southwest monsoon is still strong.

2.4. Land–Sea Breeze

Due to the varying land–sea thermal capacity of absorbing solar radiation energy, the mesoscale thermal circulation near the coast (as shown in Figure 4), which is called the land–sea breeze, occurs at many coastal locations throughout the world. Coupled with the different land–sea surface friction values and the effect of synoptic pressure gradients, the local wind circulation becomes more complex.

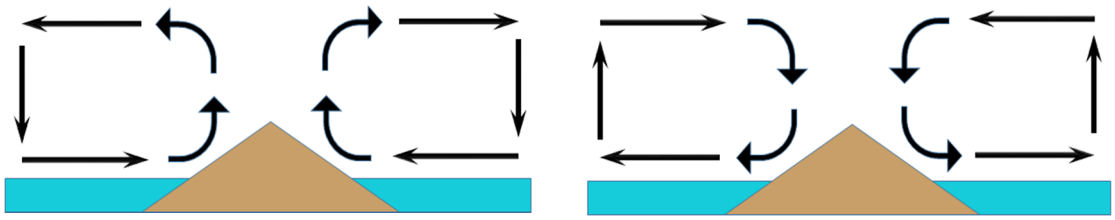

(**a**) (**b**)

Figure 4. (**a**) Sea breeze; (**b**) land breeze.

2.4.1. Sea Breeze

Sea breeze occurs during daytime and blows from the sea to the land. This is mainly because the land surface and the air above are heated by the sun, raising the air due to its low density. Moreover, because the heat storage capacity of seawater is high, the air temperature above it increases to a lesser extent, resulting in a density difference between the air above the seawater and that above the land. Consequently, the wind blows from the sea to the land. The sea breeze has the following characteristics:

- The sea breeze speed might reach 10–11 m/s at 100-m height [40].
- The height of the return flow of sea breeze ranges from hundreds of meters to 1 or 2 km.
- The wind direction of the sea breeze is constantly affected by the Coriolis force, which rotates clockwise and counterclockwise in the northern and southern hemispheres, respectively.
- The ideal land–sea breeze hodograph can be represented by an ellipse.

According to different synoptic gradients, the sea breeze can be divided into the following three models [41]:

1. Pure sea breeze

The need for a synoptic gradient is less. Sea breeze formation relies mainly on the temperature difference between air and seawater.

2. Corkscrew sea breeze

This is the strongest sea breeze model. The synoptic gradient has an offshore component, favoring sea breeze formation. For example, according to Buys Ballot's law, the formation of corkscrew sea breeze in Taiwan is favorable when the northeast monsoon is prevailing in winter.

3. Backdoor sea breezes

The synoptic gradient has an onshore component, hindering the sea breeze formation. This is the case in Taiwan summer as the south-west monsoon is prevailing.

2.4.2. Land Breeze

During the nighttime, because the heat storage capacity of the land decreases, heat dissipation increases. The air above the land surface is denser than that above the sea surface. Therefore, the wind blows toward the sea, resulting in land breeze. In the past, sailors often sailed out of the port in the morning by using land breeze.

3. Results

The wind characteristics of Formosa I offshore wind farm located in the Taiwan Strait can be roughly understood from the annual mean and standard deviation of wind speed and the wind rose.

- The average wind speed at 90-m height is approximately 8 m/s, but the standard deviation is >5.5 m/s.
- The exponent of the vertical profile of horizontal wind is approximately 0.05, which is relatively low.
- The prevailing wind direction is obvious and concentrated and strongly correlated with the season. The prevailing wind directions in winter and summer are almost opposite.
- Wind turbines may be fully loaded (wind speed > 12 m/s) > 30% of the year.

We clearly understand the phenomenon that the standard deviation is somewhat high to the corresponding mean wind speed, and there is a notable amount of full load (>12 m/s) time for the moderate mean wind speed (<8 m/s). The monthly mean and standard deviation of wind speed and the hourly mean wind speed and direction in a month were further investigated.

3.1. Monthly Mean and Standard Deviation of Wind Speed

The annual mean wind speed at 90-m height approximately equals the mean summer wind speed (Figure 5). However, the mean wind speed in winter can increase to 12 m/s with an even higher standard deviation, yielding numerous high-speed winds and light winds.

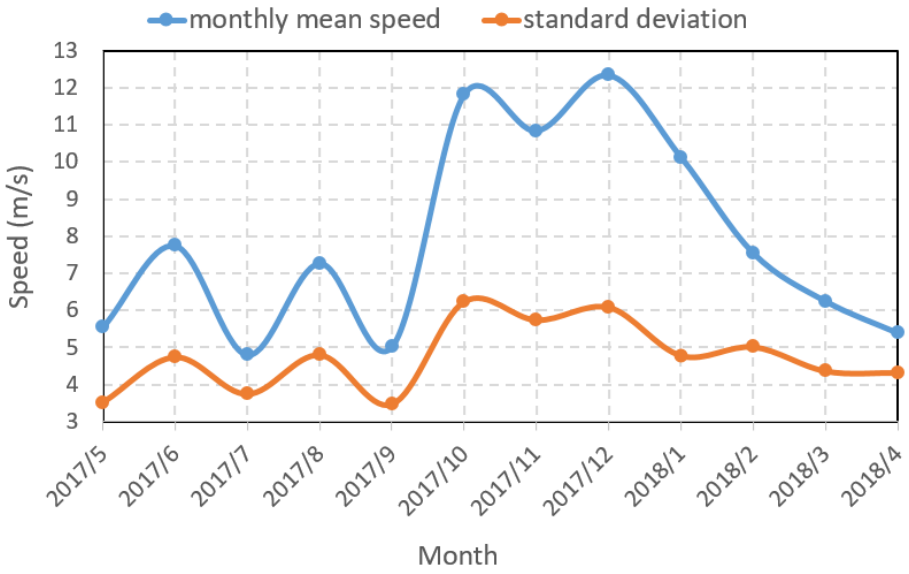

Figure 5. Monthly mean and standard deviation of wind speed at the 90-m height.

The fluctuation of the monthly mean wind speed in May, June, July, and August is caused by the variation in the southwest monsoon intensity. Similarly, changes in the northeast monsoon intensity cause the monthly mean wind speed to oscillate in October, November, and December. However, to conclude whether these phenomena occur every year, more time series data are needed for investigation.

3.2. Hourly Mean Wind Speed and Direction in a Month

Although monthly means and standard deviations of wind speed help to understand the seasonal effect on the wind speed, hourly variation in the wind speed in each month provides diurnal changes. Due to space limitations, only the results of June and December are shown, representing summer and winter, respectively. December has the highest monthly mean wind speed in a year. June is halfway from December and has no special incidents (typhoons strike). Two typhoons (Typhoons Nesat and Haitang) passed by the Formosa I offshore wind farm as they hit Taiwan in July 2017.

The highest wind speed of a day occurs in the afternoon both in winter and summer, and the highest wind speed of a year occurs in the winter afternoon (Figure 6). Moreover, the lowest wind speed in a year often occurs at night and early morning in the summer. The daily mean angular

variation of wind direction in summer is approximately 40° compared with that in winter, which is only approximately 25°.

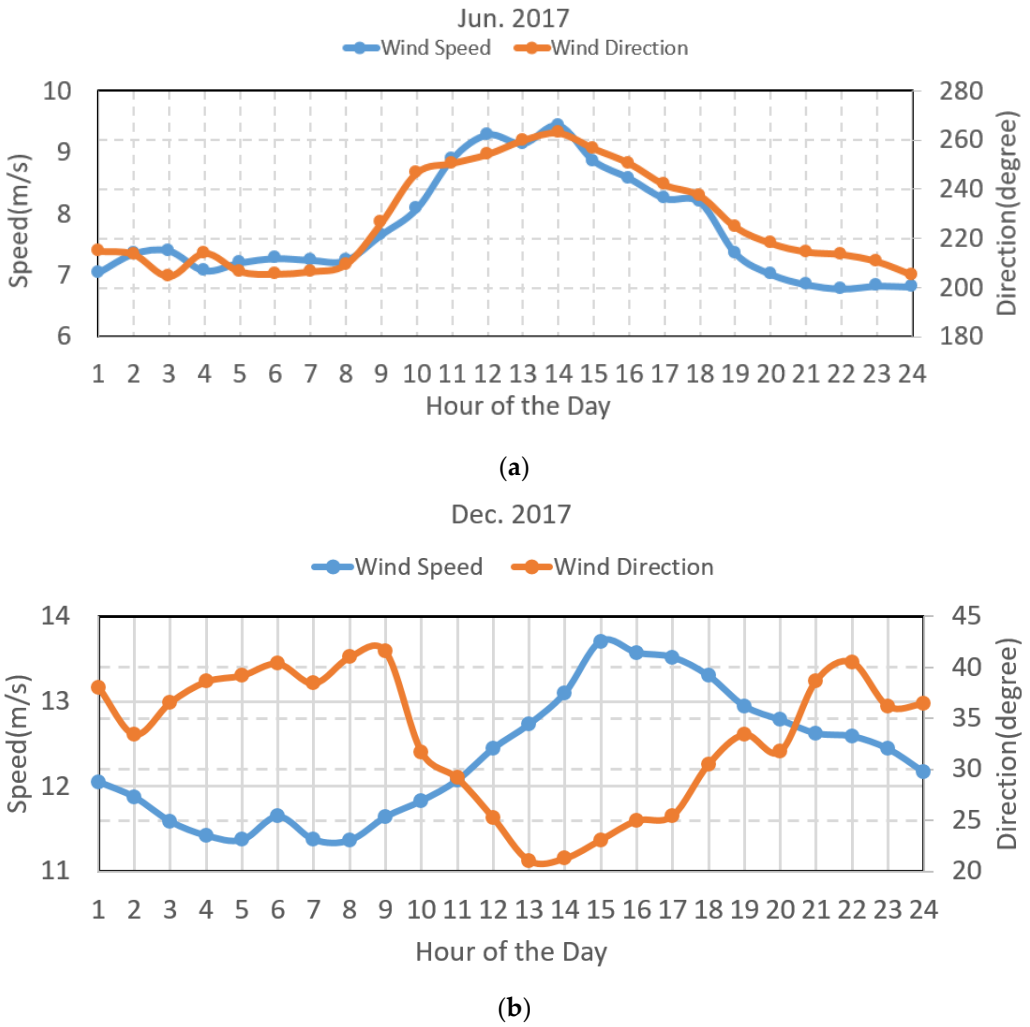

Figure 6. (**a**) Hourly mean wind speed and direction at 90-m height in June 2017. (**b**) Hourly mean wind speed and direction at 90-m height in December 2017.

3.3. Probability Distribution Modeling of Wind Speed

Wind speed at different heights can be fit to certain probability density functions to fully describe its statistical characteristics and be used for wind power potential assessment. Figure 7 illustrates the relative frequency histograms and the fitted Weibull density functions of the wind speed at different heights of the met mast. Wind speed data were fit to a Weibull probability density function owing to its high popularity for depicting wind speed distribution.

For the wind speed data at the 90-m height (see Figure 7a), the maximum likelihood estimates of the scale and shape parameters are 8.75 and 1.44, respectively. Although the fitted distribution yields expected value (7.95) and variance (31.45) very close to the sample mean (7.94) and sample variance (30.77), it is also evident that the fitted Weibull density is lower than the sample density in the low wind speed range (1 m/s to 4 m/s) and high wind speed range (12 m/s to 16 m/s), and is higher than the sample density in the median wind speed range (5 m/s to 10 m/s). A further check on the coefficient of skewness found that the coefficient of skewness of the observed wind speed data (0.696) is much lower than that of the fitted Weibull density function (1.148). Similar patterns of the sample wind speed distribution and fitted Weibull density function can also be observed for wind speed data at

other heights. Such mismatch suggests that the univariate Weibull density function is not appropriate for characterizing the wind speed data in our study site.

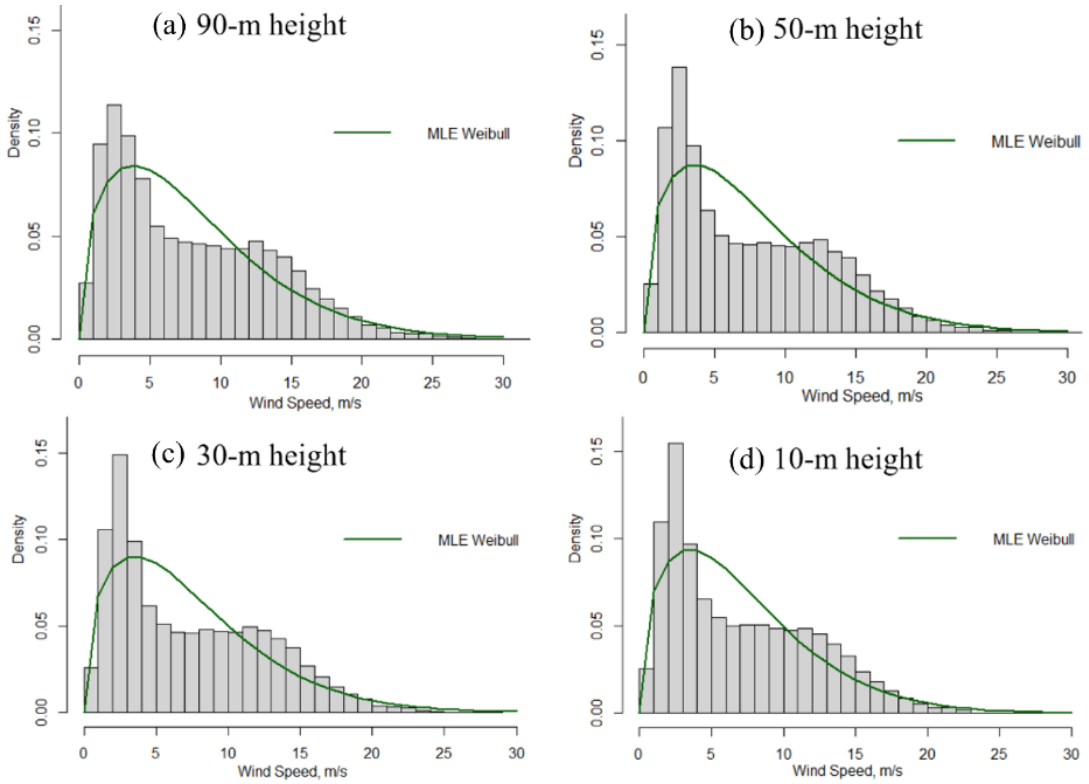

Figure 7. The relative histogram and fitted Weibull density of the wind speed at different heights (**a**) 90 m, (**b**) 50 m, (**c**) 30 m, (**d**) 10 m.

Statistical properties of the wind speed data and the parameter values of their corresponding fitted Weibull density functions are summarized in Table 1.

Table 1. Statistical properties of the wind speed data and the fitted Weibull distributions.

	Observed Data		**Fitted Weibull Distribution**	
	Sample Mean	***Sample Variance***	***Shape Parameter***	***Scale Parameter***
90-m	7.94	30.77	1.44	8.75
50-m	7.63	29.31	1.42	8.40
30-m	7.40	27.27	1.43	8.16
10-m	7.11	24.93	1.44	7.86

A more detailed examination of the sample relative frequency histogram indicates that the wind speed data may have a bimodal distribution with one peak near 3 m/s and another near 13 m/s. Thus, the two-component mixture Weibull distribution and mixture gamma distribution were also fitted to wind speed data of different heights. Figure 8 demonstrates the fitted probability density function of the mixture gamma, mixture Weibull, and univariate Weibull distributions. Both the mixture gamma distribution and mixture Weibull distribution well represent the bimodal pattern of the wind speed data. Parameters of the fitted mixture gamma and mixture Weibull distributions are summarized in Table 2.

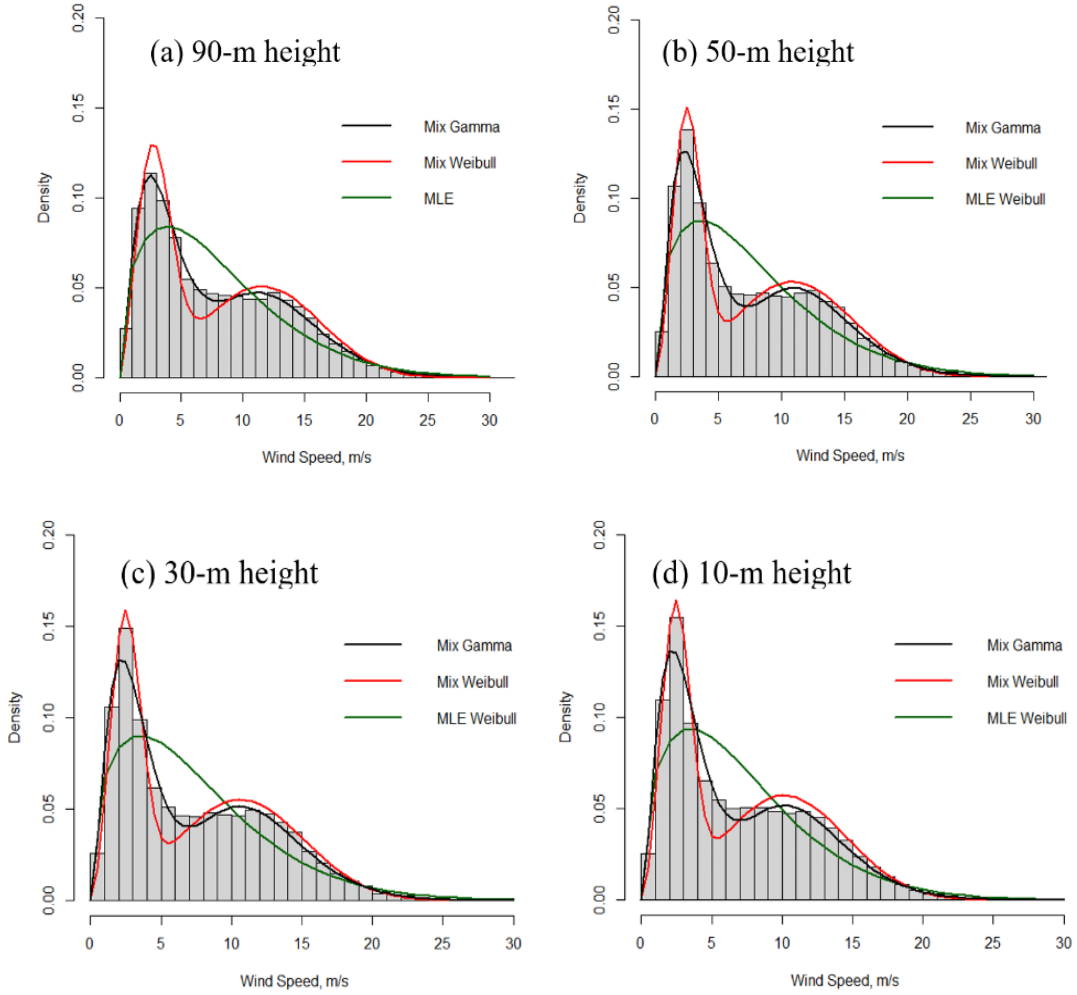

Figure 8. Fitted density functions of the mixture gamma, mixture Weibull, and univariate Weibull (maximum likelihood method) distributions for wind speed data at different heights. (**a**) 90 m, (**b**) 50 m, (**c**) 30 m, (**d**) 10 m.

Table 2. Parameters of the fitted mixture Weibull and mixture gamma distributions for the wind speed data at different heights.

	90 m		50 m		30 m		10 m	
	Mixture Weibull	**Mixture Gamma**	**Mixture Weibull**	**Mixture Gamma**	**Mixture Weibull**	**Mixture Gamma**	**Mixture Weibull**	**Mixture Gamma**
weight 1	0.41	0.56	0.40	0.54	0.40	0.54	0.40	0.56
weight 2	0.59	0.44	0.60	0.46	0.60	0.46	0.60	0.44
scale 1	3.28	1.45	2.92	1.15	2.88	1.10	2.83	1.10
shape 1	2.45	2.70	2.68	2.98	2.76	3.00	2.81	3.00
scale 2	13.29	1.30	12.65	1.25	12.30	1.20	11.78	1.15
shape 2	2.94	10.06	2.83	10.00	2.87	10.06	2.85	10.12

3.4. Model Selection Based on the Akaike Information Criterion

In order to select the best fit distribution among the univariate Weibull, the mixture Weibull, and the mixture gamma distribution, the Akaike information criterion (AIC) was adopted in this study.

A random sample of size n, i.e., $x_1, x_2, \cdots, x_n$, can be fitted by different probability distributions with estimated parameters $\hat{\theta}$. The AIC of the fitted distribution of the given sample is calculated by [42]

$$\mathrm{AIC} = 2p - 2\ell\left(\hat{\theta}\right) \tag{17}$$

where p is the number of parameters of the fitted distribution and $\ell\left(\hat{\theta}\right)$ is the log-likelihood of the random sample under the fitted distribution (See Equation (16)). The best fit model yields the lowest AIC values.

Table 3 shows the AIC values of the fitted distributions (univariate Weibull, mixture Weibull, and mixture gamma) for wind speed data at different heights. The two mixture distribution models clearly outperform the univariate Weibull distribution and the mixture gamma distribution yields the lowest AIC value for wind speed data at all different heights.

Table 3. The Akaike information criterion (AIC) values of different distribution models for wind speed data at different heights.

	Univariate Weibull	Mixture Weibull	Mixture Gamma
90-m	279,511.3	276,008.5	274,712.3
50-m	276,397.7	270,508.6	269,725.8
30-m	273,244.2	266,738.6	266,213.6
10-m	269,025.7	263,178.7	262,612.3

3.5. The Interaction between Land–Sea Breezes and Monsoons

The analysis of daily variation in wind speed and direction indicates the following features:

- Daily wind direction oscillation basically centers on the prevailing wind direction.
- The stronger the prevailing wind speed is, the smaller the variation in wind direction.

In addition, considering the bimodal probability density function, the distance between the met mast and the coastline, and the land–sea breeze cyclically rotating in a day, the wind field, consisted of resultant wind vectors, appears to be highly affected by the monsoon and land–sea breeze.

3.5.1. In Winter

Taiwan has a noticeable northeast monsoon in winter. Generally, the wind speed on the ground could surpass Beaufort number 5 (or 8.0–10.7 m/s) and even reach Beaufort number 10 (or 24.5–28.4 m/s). The following are an idealized land–sea breeze hodograph and a northeast monsoon (with a wind orientation of 30°), with the illustrations of daily variations in the mean wind speed and wind direction for the month. We used December 2017 as an example (Figure 6b). The angle between the coastline nearby the met mast and the north is approximately 35–40° (Figure 1). Schematics are shown with invariable monsoon and ellipse. The following should at least be considered in a real hodograph:

- The wind speed and direction of the northeast monsoon are not constant and change with time.
- The speed intensity of land–sea breeze wind varies due to the temperature difference between the sea surface and the ground. For example, in winter the sunshine is weaker and shorter; thus, the ground temperature is low in the early morning and evening, hence the sea breeze is usually weaker in winter than that in summer.
- Changes in the wind direction caused by terrain.
- The speed of the land breeze during nighttime is frequently lower than that of the sea breeze during daytime. Therefore, the minor axis of the night part of the ellipse is shorter than that of the ideal ellipse.

In Figure 9, the blue arrow represents the northeast monsoon in winter, and the land–sea breeze arrow rotates in the ellipse, with different colors for different times of the day. The gray arrow represents the wind speed resultant vector composed of the land–sea breeze and the winter monsoon. First, Figure 9a shows that the angle of the wind direction at 9 am is close to the maximum angle of the day (approximately 40°). Then, Figure 9b shows that the wind speed reaches the maximum value of the whole day at 3 pm, and the angle of the wind direction also gradually rises from the minimum

value. Figure 9c shows that the wind speed is still strong at 9 pm, but the wind direction returns to the maximum value of the whole day.

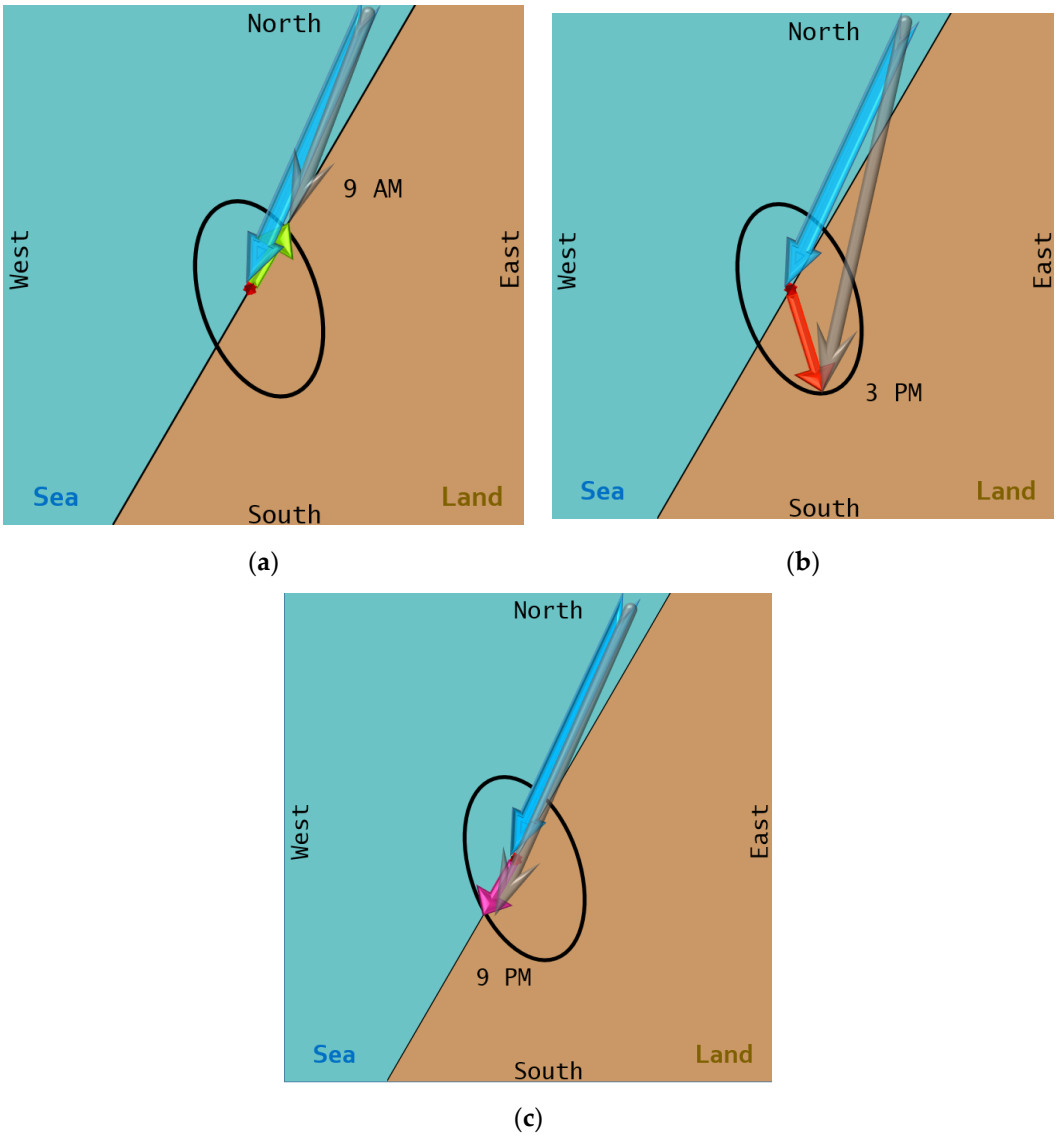

Figure 9. The blue arrows represent the northeast monsoon in winter. The land–sea breeze arrows rotate in the ellipse are shown with different colors for different times (9 AM, 3 PM, 9 PM) on a winter day. The gray arrows represent the wind speed resultant vectors composed of the land–sea breeze and the winter monsoon. (**a**) Resultant wind vector at 9 AM in December; (**b**) resultant wind vector at 3 PM in December; (**c**) resultant wind vector at 9 PM in December.

3.5.2. In Summer

The southwest monsoon often occurs in summer in Taiwan, and the wind speed is usually <8.0 m/s. When monsoon prevails, the wind speed can reach an approximate Beaufort number 5 (or 8.0–10.7 m/s) but rarely exceeds Beaufort number 6 (or 10.8–13.8 m/s). We used June 2017 as an example (Figure 6a).

In Figure 10, the red arrow represents the summer southwest monsoon, and the gray arrow represents the wind speed resultant vector composed of the land–sea breeze and the summer monsoon. First, Figure 10a shows that the angle of the wind direction at 7 am is close to the minimum angle of the day (approximately 210°). Next, Figure 10b shows that the wind speed reaches the maximum value of the whole day at 2 pm, when the angle of the wind speed reaches the maximum value of the whole day

(approximately 260°). Finally, Figure 10c shows that when the wind direction has returned to nearly parallel to the coastline at 7 pm, when the wind speed drops and approaches the minimum value.

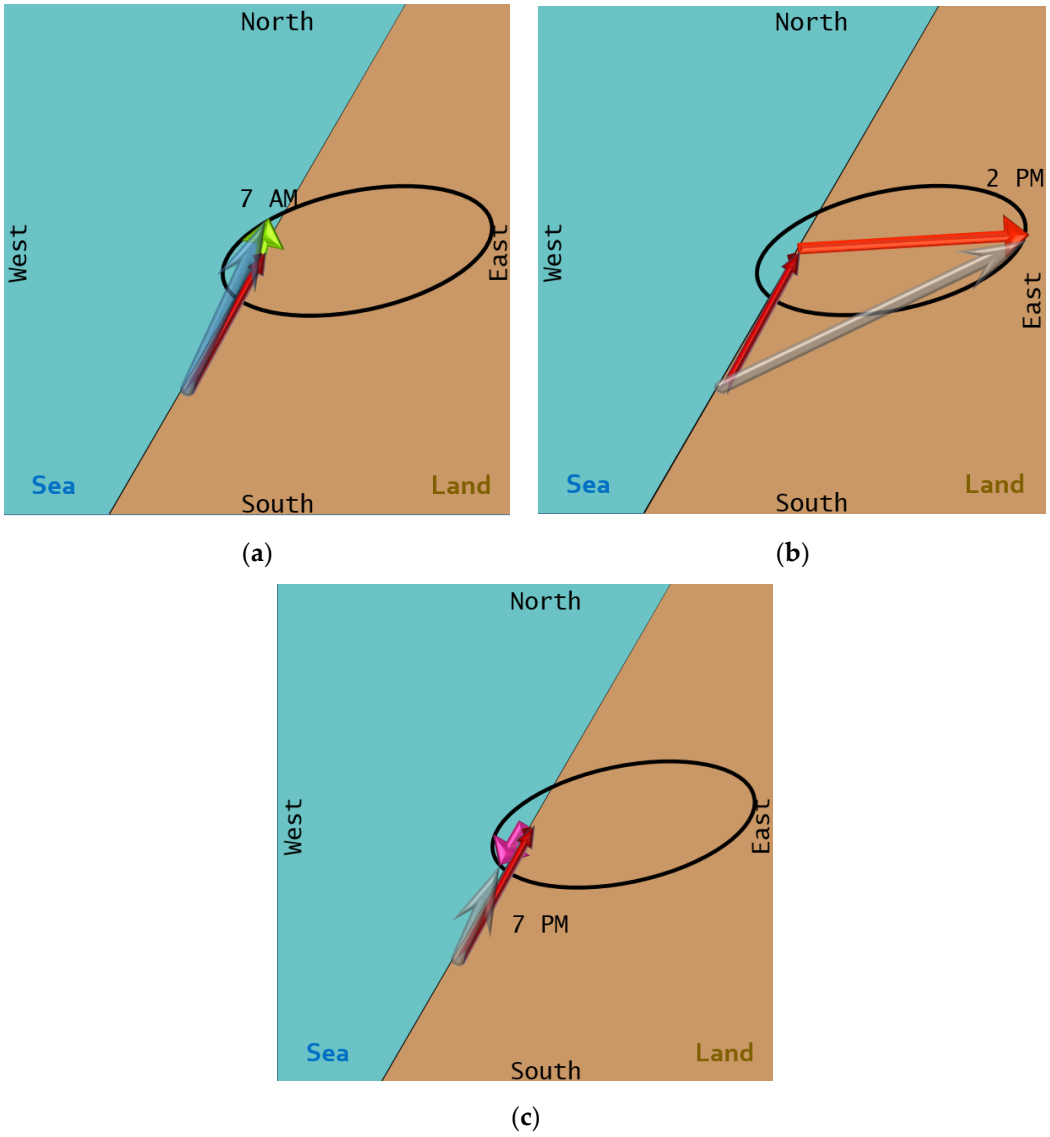

Figure 10. The blue arrows represent the southwest monsoon in summer. The land–sea breeze arrows rotate in the ellipse are shown with different colors for different times (7 AM, 2 PM, 7 PM) on a summer day. The gray arrows represent the wind speed resultant vectors composed of the land–sea breeze and the summer monsoon. (**a**) Resultant wind vector at 7 AM in June; (**b**) resultant wind vector at 2 PM in June; (**c**) resultant wind vector at 7 PM in June.

On the basis of the above illustrations, the bimodal probability distribution function is probably induced by the land–sea breeze, which speeds up or slows down the prevailing monsoon.

3.6. Low Hellmann Exponent

The composition of monsoon and land–sea wind vectors also alters the shape of the wind profile, and the exponent of the power law changes accordingly. Particularly, when subtracting two wind vectors of comparable magnitude and the smaller one having a larger exponent, the resultant wind profile will have a lower exponent. This situation is common in summer (Figure 10c). For example, when the southwest monsoon wind speed along the coastline is 2 m/s and the exponent is 0.1, whereas sea breeze speed along the coastline toward the southwest is 1.2 m/s with 0.14 exponents,

the exponent of the resultant wind profile is then 0.046. This may partly be the reason for the low exponent of the wind field. A detailed explanation regarding the low Hellmann exponent is provided in the Discussion section.

4. Discussion

We can further explore impacts of the above results on wind energy production and present recommendations regarding wind energy assessment, wind farm siting, wind turbine selection, and wind energy forecasting.

4.1. Annual Energy Production (AEP)

The AEP of a wind turbine is the total amount of electrical energy it produces over a year, which is measured in megawatt hours or gigawatt hours (MWh or GWh). Similarly, AEP can be described as an index for assessing the economic feasibility of a commercial wind turbine for electricity generation. Accordingly, this index can be estimated by multiplying the power for each wind speed from the power curve with the wind speed frequency distribution experienced by the wind turbine, and the number of hours in a year.

$$\mathrm{AEP} = 8760 \int_{v_{ci}}^{v_{co}} Pt(v) f(v) dv \tag{18}$$

where AEP is the annual energy production. *Pt(v)* is the power output curve of a wind turbine. v_{ci} is the cut-in wind speed (minimum wind speed for the wind turbine to operate), and v_{co} is the cut-out wind speed (maximum wind speed before being turned off the wind turbine for equipment protection).

However, power curves are proprietary of manufactures and are therefore difficult to obtain. Hereby, we used the power curve of an 8-MW reference wind turbine from the EU FP7 project LEANWIND [43] with the identical cut-in and cut-out speeds as that of the wind turbine deployed in Formosa 1 offshore wind farm. The power curve is illustrated in Figure 11.

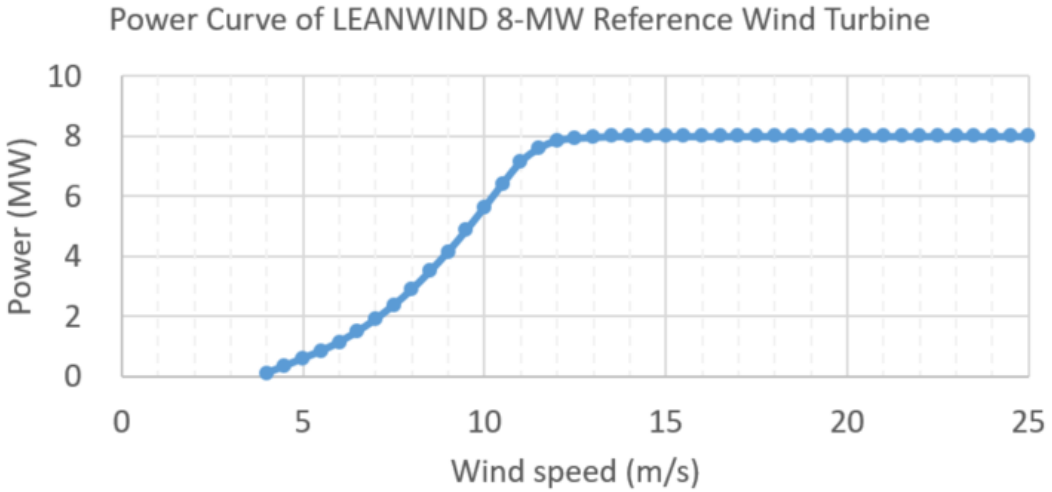

Figure 11. The power curve of LEANWIND 8MW reference wind turbine.

As soon as the AEP is determined, the capacity factor C_f can be calculated using the ratio of the AEP to the rated power output *Pr* over a period of an entire year as follows:

$$\mathrm{C}_f = \frac{\mathrm{AEP}}{8760 * P_r} \tag{19}$$

In our case, the rated AEP is 70.08 GWh when the wind turbine works at full capacity for the entire year. As shown in Table 4, the AEP and capacity factor of the mixture gamma function are 28.73% and 40.99%, respectively, which is the best fitting function because of the closest approximation to the values

calculated using the histogram. Univariate Weibull distribution function is undervalued by approximately 6.8%. Contrarily, the mixture Weibull distribution function is overrated by approximately 7.1%.

Table 4. Annual energy production and capacity factor.

	Histogram	Univariate Weibull	Mixture Weibull	Mixture Gamma
AEP(GWh)	28.81	26.85	30.86	28.73
Capacity Factor	41.10%	38.31%	44.03%	40.99%

4.2. Operating Probability of Wind Turbines

The operating probability is the difference in probabilities between the cut-in and cut-out wind speeds. The calculation introduces merely the features of the probability density function, making it another indicator for selecting wind turbines based on economic feasibility.

$$P_{op} = \int_{v_{ci}}^{v_{co}} f(v)dv \tag{20}$$

The Formosa I offshore wind farm deploys 20 Siemens Gamesa 6-MW SWT-6.0-154 wind turbines. Its cut-in and cut-out wind speeds are 4.0 and 25.0 m/s, respectively. Substitute mixture distributions into the aforementioned equation for calculating the probability between the cut-in and cut-out wind speeds. Table 5 shows that the operating probability of the mixture gamma function is 68.62%, which is relatively close to the value obtained by a histogram. Contrary to the AEP results, univariate Weibull distribution function is overrated by approximately 6.8%, and the mixture Weibull distribution function is undervalued by approximately 1.5%.

Table 5. Operating probability for distributions.

	Histogram	Univariate Weibull	Mixture Weibull	Mixture Gamma
Operating Probability	68.72%	73.41%	67.69%	68.62%

4.3. Strength, Direction, Depth and Extension of Land–Sea Breeze

The magnitude and direction of the land–sea breeze affect the resultant wind speed that actually drives wind turbines, which determines the capacity of wind power production. The peak electricity consumption period in Taiwan is summer afternoons. If the sea breeze speed is insufficient or even absent (Figure 10b), acquiring the power produced by other energy sources in advance is necessary to avoid grid instability.

Land–sea breeze influences the speed gradient (i.e., exponent) of the resultant wind profile, accordingly affecting the shear stress imposed on wind turbine blades. Additionally, the extent to which the land–sea breeze depth encompasses the swept area of blades is related to the estimation of the shear stress on the blades.

The distance and strength of the land–sea breeze are both important factors for the site selection of offshore wind farms. Therefore, the strength, direction, depth, and extension distance of the land–sea breeze are the topics of in-depth study.

4.4. Hellmann Exponent

From the aforementioned analysis, the wind profile exponent is low, which may be caused by the following:

4.4.1. Composition of Monsoons and Land–Sea Winds

Under certain conditions, the composition of wind speeds will cause the Hellmann exponent to decrease, refer to Section 3.6 for details.

4.4.2. Atmospheric Instability above the Sea Surface

The Hsinchu buoy, set up by the Central Weather Bureau approximately 6 km northeast to the met mast, provides seawater and air temperatures from 12:00 a.m. to 9:00 a.m. The temperature difference between the air (Ta) and the seawater (Tw) in summer is smaller than that in winter (Figure 12). However, even in the early spring mornings, the temperature of the seawater is higher than that of the air, which means that the ocean surface keeps heating the air.

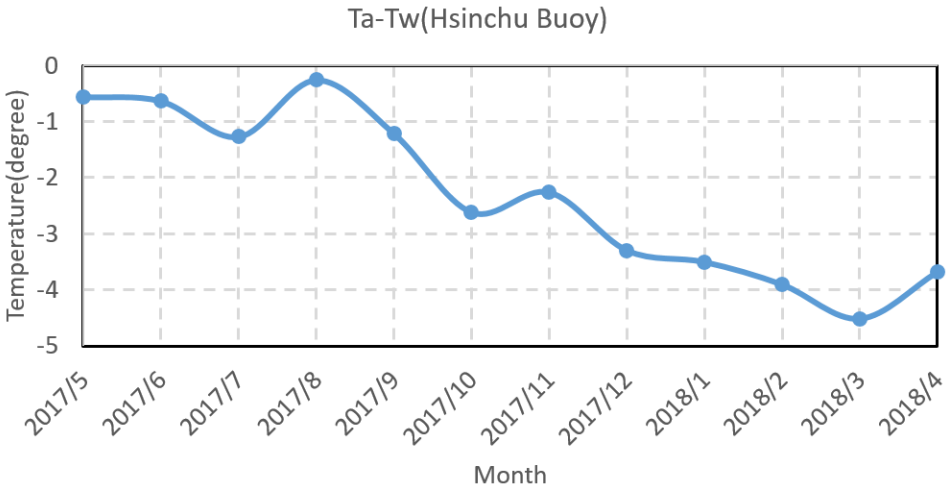

Figure 12. Temperature difference between the air and the sea surface.

4.4.3. Channel Effect Caused by the Contraction of the Taiwan Strait

Figure 1a shows that the met mast in this study is located nearby the narrowest section of the Taiwan Strait, by which the wind accelerated, leading to the internal momentum exchange.

The latter two reasons indicate that the frequent momentum exchange among the upper and lower layers exists inside the wind field, combined with the first reason, hereby making the Hellmann exponent low.

4.5. Wind Energy Forecast

For improving wind energy forecasting, the following factors are recommended:

- Temperature difference between the sea surface and the ground to assist the assessment of the formation and strength of land–sea winds.
- Temperature difference between the air above the sea and the sea surface to assist the evaluation of the possible changes in the vertical wind profile by the atmospheric stability.

5. Conclusions

This study analyzed the wind speed data of the met mast located at the Formosa I offshore wind farm from May 2017 to April 2018 to understand the wind characteristics of the Taiwan Strait:

- The annual mean wind speed at 90-m height is approximately 8 m/s, but the standard deviation is >5.5 m/s. The wind speed has a somewhat large spreading.
- Two prevailing wind directions exist, which are almost opposite, namely the north-east monsoon in winter and the south-west monsoon in summer. The intensity of the north-east monsoon is usually greater than that of the southwest monsoon.
- Winter afternoon has the highest wind speed of the year. Conversely, summer night and early morning have the lowest wind speed of the year.
- The exponent of the vertical profile of the horizontal wind is low at approximately 0.05.

Compared with Weibull distribution, the histogram has a higher distribution probability for wind speeds < 4 and > 11 m/s and a lower distribution probability for wind speeds from 4 to 11 m/s. It appears to be a bimodal distribution. Therefore, a mixture distribution consisting of two distributions is used to fit the histogram. The mixture gamma distribution has the best performance for depicting wind data, which is confirmed by Sections 4.1 and 4.2. In addition to the diurnal variation of wind speed with associated changes in wind direction (Figure 6), the met mast is only approximately 5 km away from the coastline. Thus, the wind field near this wind farm is greatly affected by the monsoon and land–sea breeze. Land–sea breeze affects not only the wind speed but also the vertical gradient of the wind.

On the basis of the aforementioned findings, we can conclude two more wind characteristics of the Taiwan Strait.

- The bimodal probability distribution function depicts wind accurately. A correct probability distribution function is crucial. Only with the correct probability distribution function can we correctly assess the wind energy potential and select an economically feasible site. Accordingly, after selecting the wind turbine, the AEP can be calculated correctly.
- The strength and direction of the land–sea breeze have significant effects on Taiwan's peak electricity consumption hours in the summer afternoons.

To improve the accuracy of wind energy forecasting, two factors should be considered: the temperature difference between the sea surface and the ground and the temperature difference between the air above the sea and the sea surface. Indubitably, to better understand the effect of land–sea breeze on wind power production, it is highly recommended to conduct an extensive land–sea breeze observation experiment and to integrate high-resolution numerical weather prediction models so as to thoroughly understand the strength and extension of land–sea breeze.

In the future, we hope to obtain high sampling frequency wind data to evaluate the effect of wind speed extremes on the structural safety of wind turbine blades. Additionally, because the vertical gradient of wind speed and the wave height will mutually interact with each other, the extreme value will help to estimate the wave height accurately [44], thus providing an accurate vertical gradient of wind speed. For the sustainability operation of wind farms, long-term observation data collected together with the model output (such as reanalysis data) will help to evaluate the wind climate transition, which is certainly a worthwhile research issue [19,45–47].

Author Contributions: Conceptualization, K.-S.C., C.-Y.H. and J.-H.T.; methodology, K.-S.C. and C.-Y.H.; software, K.-S.C. and C.-Y.H.; validation, K.-S.C. and C.-Y.H.; formal analysis, K.-S.C.; investigation, C.-Y.H.; resources, K.-S.C.; data curation, C.-Y.H.; writing—original draft preparation, C.-Y.H.; writing—review and editing, C.-Y.H.; visualization, C.-Y.H. and J.-H.T.; supervision, K.-S.C.; project administration, C.-Y.H.; funding acquisition, C.-Y.H. All authors have read and agreed to the published version of the manuscript.

Funding: This research was funded by the Ministry of Science and Technology, grant number: MOST 109-2221-E-002-016.

Acknowledgments: The authors would like to express their sincere gratitude to the Bureau of Energy for the provision of wind data. The authors are also grateful for the funding granted by the Ministry of Science and Technology. The authors would also like to thank Teng-Wei Lin and Hway-Min Chou for their help in coding, as well as Wen-Hsuan Chen for his effort in visualization. We gratefully acknowledge the input of three anonymous reviewers, which greatly improved the paper.

Conflicts of Interest: The authors declare no conflict of interest.

References

1. Renewable Energy Economics. Available online: https://www.bp.com/en/global/corporate/energy-economics/statistical-review-of-world-energy/renewable-energy.html#wind-energy (accessed on 1 November 2020).
2. Musial, W.; Beiter, P.; Nunemaker, J.; Gevorgian, V.; Cooperman, A.; Hammond, R.; Shields, M.; Spitsen, P. *2019 Offshore Wind Technology Data Update*; National Renewable Energy Laboratory: Golden, CO, USA, 2020.
3. Offshore Wind-Power Generation. 2019. Available online: https://english.ey.gov.tw/News3/9E5540D592A5FECD/34ff3d6b-412e-458d-afe9-01737d2da52d (accessed on 1 November 2020).

4. MOEA Plans a New Target to Develop Further 10 GW of Offshore Wind Capacity between 2026 to 2035—Anticipation of a Price Drop below the Average Consumer Price. 2020. Available online: https://www.moeaboe.gov.tw/ECW/english/news/News.aspx?kind=6&menu_id=958&news_id=16566 (accessed on 1 November 2020).
5. Carta, A.J.; Ramirez, P.; Velazquez, S. A review of wind speed probability distributions used in wind energy analysis: Case studies in the Canary Islands. *Renew. Sustain. Energy Rev.* **2009**, *13*, 933–955. [CrossRef]
6. Morgan, E.C.; Lackner, M.; Vogel, R.M.; Baise, L.G. Probability distributions for offshore wind speeds. *Energy Convers. Manag.* **2011**, *52*, 15–26. [CrossRef]
7. Zhang, J.; Chowdhury, S.; Messac, A.; Castillo, L. A Multivariate and Multimodal Wind Distribution model. *Renew. Energy* **2013**, *51*, 436–447. [CrossRef]
8. Soukissian, T. Use of multi-parameter distributions for offshore wind speed modeling: The Johnson SB distribution. *Appl. Energy* **2013**, *111*, 982–1000. [CrossRef]
9. Breton, S.-P.; Moe, G. Status, plans and technologies for offshore wind turbines in Europe and North America. *Renew. Energy* **2009**, *34*, 646–654. [CrossRef]
10. Neumann, J. On the Rotation Rate of the Direction of Sea and Land Breezes. *J. Atmos. Sci.* **1977**, *34*, 1913–1917. [CrossRef]
11. Lin, C.-J.; Yu, O.S.; Chang, C.-L.; Liu, Y.-H.; Chuang, Y.-F.; Lin, Y.-L. Challenges of wind farms connection to future power systems in Taiwan. *Renew. Energy* **2009**, *34*, 1926–1930. [CrossRef]
12. Huang, Y.-H.; Wu, J.-H. A transition toward a market expansion phase: Policies for promoting wind power in Taiwan. *Energy* **2009**, *34*, 437–447. [CrossRef]
13. Chen, F.; Lu, S.-M.; Tseng, K.-T.; Lee, S.-C.; Wang, E. Assessment of renewable energy reserves in Taiwan. *Renew. Sustain. Energy Rev.* **2010**, *14*, 2511–2528. [CrossRef]
14. Tsai, W.-T. Energy sustainability from analysis of sustainable development indicators: A case study in Taiwan. *Renew. Sustain. Energy Rev.* **2010**, *14*, 2131–2138. [CrossRef]
15. Wu, K.Y.; Lee, C.-Y.; Shu, G.-H. Taiwan's first large-scale offshore wind farm connection—A real project case study with a comparison of wind turbine. *IEEE Trans. Ind. Appl.* **2011**, *47*, 1461–1469.
16. Fang, H.-F. Wind energy potential assessment for the offshore areas of Taiwan west coast and Penghu Archipelago. *Renew. Energy* **2014**, *67*, 237–241. [CrossRef]
17. Chang, P.-C.; Yang, R.-Y.; Lai, C.-M. Potential of Offshore Wind Energy and Extreme Wind Speed Forecasting on the West Coast of Taiwan. *Energies* **2015**, *8*, 1685–1700. [CrossRef]
18. Failla, G.; Arena, F. New perspectives in offshore wind energy. *Philos. Trans. R. Soc. A Math. Phys. Eng. Sci.* **2015**, *373*, 20140228. [CrossRef] [PubMed]
19. Veers, P.S.; Dykes, K.; Lantz, E.; Barth, S.; Bottasso, C.L.; Carlson, O.; Clifton, A.; Green, J.; Green, P.; Holttinen, H.; et al. Grand challenges in the science of wind energy. *Science* **2019**, *366*, eaau2027. [CrossRef]
20. Schubel, P.; Crossley, R.J. Wind Turbine Blade Design. *Energies* **2012**, *5*, 3425–3449. [CrossRef]
21. Commission, I.E. *IEC 61400-3. Wind Turbines—Part 3: Design Requirements for Offshore Wind Turbines*; International Electrotechnical Commission: Geneva, Switzerland, 2009.
22. Veritas, D.N. *DNV-OS-J101-Design of Offshore Wind Turbine Structures*; Det Norske Veritas: Oslo, Norway, 2004.
23. Veritas, D.N. *DNV-RP-C205 Environmental Conditions and Environmental Loads*; Det Norske Veritas: Oslo, Norway, 2010.
24. Kaltschmitt, M.; Streicher, W.; Wiese, A. *Renewable Energy: Technology, Economics and Environment*; Springer Science & Business Media: Berlin, Germany, 2007.
25. Albani, A.; Ibrahim, M.Z. Wind Energy Potential and Power Law Indexes Assessment for Selected Near-Coastal Sites in Malaysia. *Energies* **2017**, *10*, 307. [CrossRef]
26. Tar, K. Some statistical characteristics of monthly average wind speed at various heights. *Renew. Sustain. Energy Rev.* **2008**, *12*, 1712–1724. [CrossRef]
27. Stevens, M.; Smulders, P. The Estimation of the Parameters of the Weibull Wind Speed Distribution for Wind Energy Utilization Purposes. *Wind Eng.* **1979**, *3*, 132–145.
28. Chang, T.P. Estimation of wind energy potential using different probability density functions. *Appl. Energy* **2011**, *88*, 1848–1856. [CrossRef]
29. Carrillo, C.; Cidrás, J.; Díaz-Dorado, E.; Obando-Montaño, A.F. An approach to determine the Weibull parameters for wind energy analysis: The case of Galicia (Spain). *Energies* **2014**, *7*, 2676–2700. [CrossRef]

30. Mert, I.; Karakuş, C. A statistical analysis of wind speed data using Burr, generalized gamma, and Weibull distributions in Antakya, Turkey. *Turk. J. Electr. Eng. Comput. Sci.* **2015**, *23*, 1571–1586. [CrossRef]
31. Sedghi, M.; Hannani, S.K.; Boroushaki, M. Estimation of weibull parameters for wind energy application in Iran's cities. *Wind Struct.* **2015**, *21*, 203–221. [CrossRef]
32. Rajapaksha, K.; Perera, K.I. Wind speed analysis and energy calculation based on mixture distributions in Narakkalliya, Sri Lanka. *J. Natl. Sci. Found. Sri Lanka* **2016**, *44*, 409. [CrossRef]
33. Pobočíková, I.; Sedliačková, Z.; Michalková, M. Application of Four Probability Distributions for Wind Speed Modeling. *Procedia Eng.* **2017**, *192*, 713–718. [CrossRef]
34. Kang, D.; Ko, K.; Huh, J. Comparative Study of Different Methods for Estimating Weibull Parameters: A Case Study on Jeju Island, South Korea. *Energies* **2018**, *11*, 356. [CrossRef]
35. Erisoglu, M.; Servi, T.; Erisoglu, U.; Calis, N. Mixture Gamma Distribution for Estimation of Wind Power Potential. *Int. J. Appl. Math. Stat.* **2013**, *40*, 232–241.
36. Kite, G. *Frequency and risk analysis in hydrology*; Water Resources Publications: Littleton, CO, USA, 1988; p. 257.
37. Hamed, K.; Rao, A.R. *Flood Frequency Analysis*; CRC Press: Boca Raton, FL, USA, 2019.
38. Lindsay, B.G. Mixture models: Theory, geometry and applications. in NSF-CBMS regional conference series in probability and statistics. *JSTOR* **1995**, *5*, 53–55.
39. Hastie, T.; Tibshirani, R.; Friedman, J. *The Elements of Statistical Learning: Data Mining, Inference, and Prediction*; Springer Science & Business Media: Berlin, Germany, 2009.
40. Atkinson, B. *Meso-Scale Atmospheric Circulations*; Academic Press: San Diego, CA, USA, 1981; p. 495.
41. Adams, E. Four ways to win the sea breeze game. *Sail. World* **1997**, *3*, 412.
42. Akaike, H. A new look at the statistical model identification. *IEEE Trans. Autom. Control* **1974**, *19*, 716–723. [CrossRef]
43. Desmond, C.; Murphy, J.; Blonk, L.; Haans, W. Description of an 8 MW reference wind turbine. *J. Phys. Conf. Ser.* **2016**, *753*, 92013. [CrossRef]
44. Brown, A.G.; Neill, S.P.; Lewis, M. The influence of wind gustiness on estimating the wave power resource. *Int. J. Mar. Energy* **2013**, *3*, e1–e10. [CrossRef]
45. Olauson, J. ERA5: The new champion of wind power modelling? *Renew. Energy* **2018**, *126*, 322–331. [CrossRef]
46. Soares, P.M.; Lima, D.C.; Nogueira, M. Global offshore wind energy resources using the new ERA-5 reanalysis. *Environ. Res. Lett.* **2020**, *15*, 1040a2. [CrossRef]
47. Jung, J.; Broadwater, R.P. Current status and future advances for wind speed and power forecasting. *Renew. Sustain. Energy Rev.* **2014**, *31*, 762–777. [CrossRef]